

All-optical three-dimensional electron pulse compression

Liang Jie Wong^{1,3}, Byron Freelon², Timm Rohwer², Nuh Gedik², and Steven G Johnson¹

¹Department of Mathematics, Massachusetts Institute of Technology, 77 Massachusetts Avenue, Cambridge, Massachusetts 02139, USA

²Department of Physics, Massachusetts Institute of Technology, 77 Massachusetts Avenue, Cambridge, Massachusetts 02139, USA

³Current Address: Singapore Institute of Manufacturing Technology, 71 Nanyang Drive, Singapore 638075

E-mail: ljwong@alum.mit.edu

Abstract. We propose an all-optical, three-dimensional electron pulse compression scheme in which Hermite-Gaussian optical modes are used to fashion a three-dimensional optical trap in the electron pulse's rest frame. We show that the correct choices of optical incidence angles are necessary for optimal compression. We obtain analytical expressions for the net impulse imparted by Hermite-Gaussian free-space modes of arbitrary order. Although we focus on electrons, our theory applies to any charged particle and any particle with non-zero polarizability in the Rayleigh regime. We verify our theory numerically using exact solutions to Maxwell's equations for first-order Hermite-Gaussian beams, demonstrating single-electron pulse compression factors of $> 10^2$ in both longitudinal and transverse dimensions with experimentally realizable optical pulses. The proposed scheme is useful in ultrafast electron imaging for both single- and multi-electron pulse compression, and as a means of circumventing temporal distortions in magnetic lenses when focusing ultrashort electron pulses. Other applications include the creation of flat electron beams and ultrashort electron bunches for coherent terahertz emission.

PACS numbers: 42.65.Re, 42.50.Wk, 41.75.Fr, 61.05.J-, 07.60.Pb, 41.85.-p, 37.10.Vz

Keywords: attosecond imaging, ultrafast techniques, ultrashort electron pulses, bunch compression, beam focusing, optical traps, ponderomotive force

1. Introduction

The ability of ultrafast X-ray and electron pulses to probe structural dynamics with atomic spatiotemporal resolution has fueled a wealth of exciting research on the frontiers of physics, chemistry, biology and materials science [1–4]. Although electrons lack the penetration depth of X-rays, the large scattering cross section of electrons (10^5 - 10^6 times that of X-rays of the same energy [5,6]) and relative availability of high intensity tabletop electron sources favor the use of electrons especially in the study of surfaces, gas phase systems and nanostructures.

An electron pulse tends to expand and acquire a velocity chirp as it travels, firstly due to space-charge (i.e. inter-electron repulsion), and secondly due to dispersion resulting from an initial velocity spread. The propagation of electron pulses has been the subject of extensive study [7–9]. To ensure that the electron pulse arrives at the sample or detector with the desired properties (e.g., spot size, coherence length, pulse duration), many ultrafast electron imaging setups adopt means to compress the electron pulse transversely and longitudinally. Longitudinal compression methods include the use of electrostatic elements [10], microwave cavities [11–15] and optical transients [16,17]. These techniques can potentially compress single-electron pulses [18,19] to attosecond-scale durations [16,20]. Transverse compression, or focusing, of an electron pulse is typically achieved with standard charged particle optics like magnetic solenoid lenses. Femtosecond electron pulses, however, suffer significantly from temporal distortions in magnetic lenses and require more complicated combinations of charged particle optics for isochronic imaging [21].

In this paper, we propose a scheme for the three-dimensional compression of electron pulses using only optical transients, with no static fields involved. The scheme comprises a succession of Hermite-Gaussian optical modes that effectively fashions a three-dimensional optical trap in the electron pulse’s rest frame. Such a scheme is useful in ultrafast electron imaging for both single- and multi-electron pulse compression, and as a means of circumventing temporal distortions in magnetic lenses [21] when focusing ultrashort electron pulses. Methods of generating Hermite-Gaussian modes include the use of waveplates [22] and excitation in diode lasers [23].

In Section 2, we present an overview of the three-dimensional electron pulse compression scheme, and describe how a succession of compression stages may be implemented with a single optical pulse. In Section 3, we show mathematically that the right choice of optical incidence angle is necessary for optimal longitudinal compression, and obtain analytical expressions for the net velocity change induced in a charged particle by the passage of an optical pulse. In Section 4, we illustrate the conclusions of Section 3 with exact numerical simulations of the laser-electron interaction. We demonstrate single-electron pulse compression factors of $> 10^2$ in both longitudinal and transverse dimensions using experimentally-realizable optical pulses, and study the energy scaling laws of the compression scheme.

2. Overview

A charged particle in an electromagnetic wave experiences a time-averaged force called the ponderomotive force [24, 25] that pushes the particle towards regions of lower optical intensity in the particle's rest frame. Dielectric particles are also subject to this phenomenon, and applications of electromagnetic ponderomotive forces have included atomic cooling, optical manipulation of living organisms, plasma confinement, and electron acceleration [26–28]. The optical ponderomotive force has also been used in the characterization of ultrashort electron pulses [29–32].

Here, we use the ponderomotive force to compress an electron pulse by subjecting the electron pulse to the intensity minimums of appropriately-oriented Hermite-Gaussian modes, as illustrated in Fig. 1(a). Compression in each Cartesian dimension can be controlled without affecting electron pulse properties in orthogonal dimensions, at the lowest order. Although either Pulse I or II suffices for longitudinal compression, using two identical pulses in the configuration shown ensures that any higher-order modulations affecting transverse electron pulse properties do so equally in x and y . In Fig. 1(a), Pulses I and II control compression in z , whereas Pulses III and IV control compression in y and x respectively. The stages (and optical pulses) may be arbitrarily ordered and cascaded, as long as inter-particle interactions and dispersion affect the electron pulse negligibly between interactions. Since the ponderomotive force is a non-linear effect (i.e. not directly proportional to electric field), the optical pulses should be sufficiently far apart so that interference between the fields of different pulses does not occur.

The use of an optical pulse's transverse intensity profile for electron pulse compression has been proposed in [17]. However, the scheme in [17] uses an optical incidence angle normal to the electron path in the lab frame, a sub-optimal configuration for electrons of non-zero speed. In addition, the scheme in [17] uses a Laguerre-Gaussian “donut” mode, which – even for a stationary electron pulse – couples compression in the longitudinal dimension to that in exactly one transverse dimension.

Intuitively, the oblique optical incidence angle of the longitudinal compression stage is motivated by the desire for normal optical incidence in the electron pulse's rest frame. This implies a lab frame incidence angle of

$$\theta_1 = \arctan \left[\frac{c \sin \theta_1''}{\gamma (c \cos \theta_1'' + v)} \right] = \arctan \left(\frac{1}{\gamma \beta} \right), \quad (1)$$

where the electron pulse propagates in the $+z$ -direction with speed $v \equiv \beta c$ (c the speed of light in vacuum), corresponding to Lorentz factor $\gamma \equiv (1 - \beta^2)^{-1/2}$. The first equality in (1) expresses the relation between the rest frame incidence angle θ_1'' and θ_1 . The second equality was made by setting $\theta_1'' = 90^\circ$. We have taken the optical group velocity as c , a valid assumption [33] for the paraxial, many-cycle optical pulses we are interested in. The physics behind (1) is illustrated in Fig. 2, which shows how oblique optical incidence in the lab frame corresponds to normal optical incidence in the electron

pulse's rest frame. In the next section, we show mathematically that (1) is optimal in the sense that when it is satisfied, the induced velocity change in the longitudinal direction is not a function of transverse coordinates and not accompanied by transverse phase plane modulations, at the lowest order. Fig. 3(a) illustrates the physical mechanism of the longitudinal compression scheme: the laser-electron interaction induces a velocity modulation in the electron pulse, which then compresses as it continues to propagate. The transverse compression scheme works according to the same principles, except that the desired velocity modulation is now along a transverse dimension.

Since the electron pulse is stationary along its transverse dimensions, normal incidence in the rest frame is achieved with any value of θ_t for transverse compression. Indeed, we see in Section 4 that the transverse compression of 30 keV electrons is a relatively weak function of θ_t . However, the choice of θ_t can significantly affect the longitudinal compression ratio in a three-dimensional compression scheme via higher-order terms of the transverse compression stage, with the best results achieved when $\theta_t = 0^\circ$.

Equation (1) is also the condition for group velocity matching between electron and optical pulses along the axis of electron pulse propagation (i.e. $c\cos\theta_1 = c\beta \equiv v$). This observation motivates the cascaded compression scheme of Fig. 1(b), in which an optical pulse (either Pulse I, II, III or IV) is reflected and re-focused by a succession of optical stages, so as to be repeatedly incident upon the electron pulse, allowing the optical pulse to be utilized to its maximum capacity. If (1) is satisfied, the interval between laser-electron coincidences is

$$T_{\text{coin}} = \frac{\gamma D}{c}, \quad (2)$$

assuming that the electron pulse is injected along the axis of symmetry of the setup, and that the optical components introduce no delays. To avoid optical interference between successive interactions, D should generally be chosen so that $T_{\text{coin}} \gg \tau$ is satisfied, τ being the optical pulse duration. With suitable combinations of optics, one can also implement the design in Fig. 1(b) for any optical incidence angle, or such that a single optical pulse is used to realize several or all of Pulses I, II, III and IV, since the four types of pulses essentially differ only in orientation.

3. Theory

In this section, we obtain analytical expressions approximating the ponderomotive potential and net impulse transfer associated with transverse and longitudinal compression by pulsed Hermite-Gaussian TEM_{*mn*} modes of arbitrary order. We show mathematically that when (1) is satisfied, the induced velocity change for longitudinal compression is not a function of transverse coordinates and not accompanied by transverse phase plane modulations, at the lowest order. Although we focus on charged particles, our treatment may be extended to any particle with non-zero polarizability

in the Rayleigh regime (particle size much smaller than electromagnetic wavelength) by the simple replacement of a constant factor.

A charged particle in an electromagnetic wave experiences a force [24, 25]

$$\vec{F} = -\nabla U_p + \dots, \quad (3)$$

where the ponderomotive potential U_p is

$$U_p \equiv \frac{q^2}{4m_0\omega^2} \left| \vec{E}_a \right|^2, \quad (4)$$

and q and m_0 are respectively the particle's charge and rest mass. The particle sees the electric field $\vec{E} = (\vec{E}_a e^{i\omega t} + \text{c.c.})/2$, where \vec{E}_a varies slowly in time compared to the carrier factor and $i \equiv \sqrt{-1}$. The ellipsis in (3) hides terms proportional to $e^{\pm i\omega t}$ or $e^{\pm i2\omega t}$. Equation (3) was derived from the Newton-Lorentz equation in the rest frame of the initial particle. As such, the notion that a particle experiences a force proportional to the gradient of electromagnetic intensity is valid in the rest frame of the particle, and not necessarily in a frame where the particle moves with any substantial velocity. The net momentum imparted to a particle by the passage of a many-cycle pulse is then

$$\Delta \vec{p} = \int \vec{F} dt = - \int \nabla U_p dt, \quad (5)$$

Physically, the electric field causes the charged particle to oscillate about its initial position, generating an effective dipole that is subject to the same radiation pressure forces [34] experienced by dielectric particles in optical tweezers [26]. In fact, replacing $q/m_0\omega^2$ by $\alpha/2$ turns (4) into the ponderomotive potential of a particle in the Rayleigh regime, where the particle's polarization $\vec{P} = \alpha \vec{E}$. The results in this paper thus also apply to polarizable particles.

A paraxial, many-cycle electromagnetic pulse can be modeled using the vector potential ansatz

$$\vec{A} = \text{Re} \left\{ \vec{A} e^{i\psi} g \left(\frac{\xi}{\xi_0} \right) \right\}, \quad (6)$$

where each component of \vec{A} is a solution of the paraxial wave equation [35], $g(\cdot)$ a real even function describing the pulse shape such that $\lim_{|\xi| \rightarrow \infty} g(\xi) \rightarrow 0$, ξ_0 a constant associated with pulse duration, $\xi \equiv \omega t - k(z - z_i)$ and $\psi \equiv \xi + \psi_0$, with z_i the pulse's initial position (at $t = 0$) and ψ_0 a phase constant. x , y and z are Cartesian coordinates. \vec{A} is a slowly-varying function of only spatial coordinates such that $\partial_x \vec{A}$, $\partial_y \vec{A} = O(\epsilon_d)$ and $\partial_z \vec{A} = O(\epsilon_d^2)$, where the beam divergence angle $\epsilon_d \ll 1$. To ensure that the particle bunch interacts with the electromagnetic pulse only when the bunch is close to the electromagnetic beam axis (and hence the center of the ponderomotive potential well), we use pulses such that $\epsilon_d \ll \xi_0^{-1} \ll 1$. The electromagnetic fields are obtained via the identities [36]

$$\begin{aligned} \vec{B} &= \nabla \times \vec{A} \\ \vec{E} &= c^2 \nabla \int \nabla \cdot \vec{A} dt - \frac{\partial \vec{A}}{\partial t}, \end{aligned} \quad (7)$$

in which we have applied the Lorenz gauge.

Consider a non-zero θ ($\theta = \theta_t$ or θ_l) and a particle propagating in the $+z$ direction with speed $|\vec{v}| \equiv \beta c$. We henceforth denote all variables in the native frame of the electromagnetic pulse with prime superscripts, so the pulse propagates in the $+z'$ direction, and all variables in the particle's rest frame with double-prime superscripts. Non-primed variables x, y, z, t are lab frame variables, defined in accordance with Fig. 1(a). Note that in the rest frame, ω in (4) should be replaced by the Doppler-shifted frequency $\omega'' \equiv \omega\gamma(1 - \beta \cos \theta)$. Applying the appropriate rotation and Lorentz transformation operators to (6) and (7), we obtain the ponderomotive potential in the rest frame as

$$U_p'' = \frac{q^2}{4m_0} \left(|\tilde{A}_x|^2 + |\tilde{A}_y|^2 \right) g^2 [1 + O(\epsilon_d) + O(\xi_0^{-1}) + O(\beta)], \quad (8)$$

a result that applies for general $\vec{\tilde{A}}$ satisfying the paraxial wave equation, assuming that \tilde{A}_z is on the order of the transverse components or less.

For the linearly-polarized Hermite Gaussian TEM_{mn} mode,

$$\vec{\tilde{A}}' \equiv \hat{x}' A_0 f' \exp(-f' \rho'^2) H_m(|f'| \tilde{x}') H_n(|f'| \tilde{y}') \left(\frac{f'}{f'^*} \right)^{\frac{m+n}{2}}, \quad (9)$$

where A_0 is a normalization constant, $f' \equiv i/(i + z'/z_0)$, $\tilde{x}' \equiv \sqrt{2}x'/w_0$, $\tilde{y}' \equiv \sqrt{2}y'/w_0$, $z_0 \equiv \pi w_0^2/\lambda$ is the Rayleigh range, w_0 is the beam waist radius, $\rho' \equiv \sqrt{x'^2 + y'^2}/w_0$, and $H_m(\cdot)$ is the Hermite polynomial of order m ($H_0(x) = 1$, $H_1(x) = 2x$ etc.), with $m, n \in \mathbb{N}_0$ (the set of natural numbers including 0). The beam divergence angle is $\epsilon_d \equiv 2/(kw_0)$. From (6) and (7), the peak power P transported in the propagation direction is

$$P \equiv \iint S'_{z0} dx' dy' \approx \omega^2 A_0^2 c \epsilon_0 \pi w_0^2 2^{n+m-1} n! m!, \quad (10)$$

where S'_{z0} denotes the z -directed Poynting vector $S'_z \equiv \vec{E}' \times \vec{H}' \cdot \hat{z}'$ evaluated at the pulse peak, focal plane and carrier amplitude. ϵ_0 is the permittivity of free space. The energy U of a single pulse is related to its peak power as

$$U \equiv \iiint S'_z|_{z'=0} dx' dy' dt' \approx \frac{P}{2} \int g^2 \left(\frac{\xi'}{\xi_0} \right) d \left(\frac{\xi'}{\omega} \right). \quad (11)$$

Longitudinal compression is achieved with the TEM_{mn} mode when m is odd and n is even. In that case,

$$U_{pl}'' = \frac{m_0 K_1}{2} \left[\int g^2 \left(\frac{\xi'}{\xi_0} \right) d \left(\frac{\xi'}{\omega} \right) \right]^{-1} x'^2 g^2 \left(\frac{\xi'}{\xi_0} \right) [1 + O(\xi_0^{-1}) + O((n+m+1)\epsilon_d^2) + O(\beta)], \quad (12)$$

where

$$K_1 \equiv \frac{q^2 \lambda^2}{\pi^3 m_0^2 \epsilon_0 c^3} \frac{U}{w_0^4 2^{m+n-2} [(m-1)/2]!^2 (n/2)!^2}, \quad (13)$$

and we have applied Taylor expansions about the origin in (8) to obtain (12). The net impulse in the rest frame is then

$$\begin{aligned}\Delta \vec{p}_1'' &= - \int \nabla'' U_p'' dt'' \\ &= m_0 K_1 \frac{[\gamma (\beta - \cos \theta) \Delta x'' + \sin \theta \Delta z'']}{\gamma^2 (1 - \beta \cos \theta)^3} \left[\hat{x} (\cos \theta - \beta) - \hat{z} \frac{\sin \theta}{\gamma} \right] \\ &\quad [1 + O(\xi_0^{-1}) + O((n+m+1)\epsilon_d^2) + O(\beta)],\end{aligned}\quad (14)$$

where the particle's rest frame displacement from the bunch centroid is $(\Delta x'', \Delta y'', \Delta z'')$, which we assume does not change significantly during the interaction. To eliminate the x-directed modulation and the $\Delta x''$ -dependence of the z-directed modulation in the lowest-order term, we must choose θ such that $\cos \theta = \beta$, a condition equivalent to (1). The lab-frame velocity change is then

$$\Delta \vec{v}_1 = - \hat{z} K_1 \Delta z [1 + O(\xi_0^{-1}) + O((n+m+1)\epsilon_d^2) + O(\beta)], \quad (15)$$

where the particle's lab frame displacement from the bunch centroid is $(\Delta x, \Delta y, \Delta z)$. The longitudinal impulse in the lab frame follows from the relation $\Delta \vec{p}_1 = m_0 \gamma^3 \Delta \vec{v}_1 + O(\Delta v_1^2)$. The linear dependence in the lowest-order term of (15) corresponds to a parabolic potential profile. In the absence of space-charge and momentum spread, a particle pulse would be compressed by a perfectly parabolic potential to a zero extent.

Transverse compression is achieved with the TEM_{mn} mode when m is even and n is odd. In this case,

$$\begin{aligned}U_{pt}'' &= \frac{m_0 K_t}{2} \left[\int g^2 \left(\frac{\xi'}{\xi_0} \right) dt' \right]^{-1} y'^2 g^2 \left(\frac{\xi'}{\xi_0} \right) \\ &\quad [1 + O(\xi_0^{-1}) + O((n+m+1)\epsilon_d^2) + O(\beta)],\end{aligned}\quad (16)$$

where

$$K_t \equiv \frac{q^2 \lambda^2}{\pi^3 m_0^2 \epsilon_0 c^3} \frac{U}{w_0^4} \frac{m! n!}{2^{m+n-2} [(n-1)/2]!^2 (m/2)!^2}. \quad (17)$$

The net transverse impulse imparted by the passage of a single pulse in the rest frame is

$$\begin{aligned}\Delta \vec{p}_t'' &= - m_0 K_t \frac{1}{\gamma (1 - \beta \cos \theta)} \Delta y'' \hat{y} \\ &\quad [1 + O(\xi_0^{-1}) + O((n+m+1)\epsilon_d^2) + O(\beta)],\end{aligned}\quad (18)$$

corresponding to a net lab-frame velocity change of

$$\begin{aligned}\Delta \vec{v}_t &= - \hat{y} K_t \frac{1}{\gamma^2 (1 - \beta \cos \theta)} \Delta y \\ &\quad [1 + O(\xi_0^{-1}) + O((n+m+1)\epsilon_d^2) + O(\beta)].\end{aligned}\quad (19)$$

As θ approaches 0° , the velocity change becomes larger a result of improved group velocity matching along the optical beam axis. The transverse impulse in the lab frame follows from the relation $\Delta \vec{p}_t = m_0 \gamma \Delta \vec{v}_t + O(\Delta v_t^2)$. Several noteworthy features of the pulse compression scheme are evident from (13), (15), (17) and (19):

1. At the lowest order, net velocity change is independent of pulse duration parameter ξ_0 and pulse shape g .

2. A trade-off between the size of the parabolic potential region and the strength of the compression exists in two ways: through the laser waist radius w_0 , and through the choice of m and n . One solution to achieving a large parabolic potential region and a large Δv for a given total optical energy may lie in the superposition of higher-order Hermite-Gaussian modes, as proposed in [37] in the context of atomic beam imaging.

3. That $\Delta v \propto \lambda^2$ (as expected of a ponderomotive force scheme [25]) suggests that greater net impulse may be achieved via longer-wavelength sources. Note, however, that increasing the wavelength increases the pulse duration for the same number of temporal cycles, which may weaken the assumption that the particle's position relative to the intensity well does not change significantly during the interaction.

The focal time (the time of maximal compression) of a particle pulse with a velocity chirp can be estimated with the formula

$$t_f = \frac{\Delta r_0}{|v_T|}, \quad (20)$$

where $v_T \equiv \Delta v + v_0$. Δr_0 and v_0 refer respectively to the half-width of the particle pulse and the velocity of a particle at the pulse's edge, along the dimension of compression and immediately before the interaction. Δv is the velocity change induced in the particle at the pulse's edge as a result of the interaction.

4. Numerical simulations

To numerically model the laser-electron interaction, we solve the exact Newton-Lorentz equation using an adaptive-step fifth-order Runge-Kutta algorithm [38]. The coordinates of each particle are assigned in a quasi-random fashion using Halton sequences [38]. For the laser pulses, we employ first-order Hermite-Gaussian modes that are exact (i.e. non-paraxial) solutions of Maxwell's equations in free space. We readily obtain the fields of a TEM_{10} mode with a Poisson spectrum by using the Hertz vector potential

$$\vec{\Pi}_{10} = \frac{\partial}{\partial x} \vec{\Pi}_{00} \quad (21)$$

in the relations [39]

$$\begin{aligned} \vec{B} &= \text{Re} \left\{ \frac{1}{c^2} \frac{\partial}{\partial t} \nabla \times \vec{\Pi}_{10} \right\} \\ \vec{E} &= \text{Re} \left\{ \nabla \times \nabla \times \vec{\Pi}_{10} \right\}. \end{aligned} \quad (22)$$

The vector potential corresponding to a fundamental Gaussian mode is [40, 41]

$$\vec{\Pi}_{00} = \hat{x} \Pi_0 \frac{1}{R'} (f_+^{-s-1} - f_-^{-s-1}), \quad (23)$$

where $f_{\pm} = 1 - (i/s)(\omega t \pm kR' + ika)$, $R' = [x^2 + y^2 + (z + ia)^2]^{1/2}$, and Π_0 is a complex constant. The degree of focusing and the pulse duration are controlled through parameters a and s via relations for which good analytical approximations have been derived [40,41]. The non-paraxial Gaussian beam reduces to the phasor of the paraxial Gaussian beam in the paraxial limit [42], so the description (21)-(23) is consistent with (6)-(9).

Unless otherwise specified, all numerical simulations use optical pulses of wavelength $\lambda = 0.8\mu\text{m}$, waist radius $w_0 = 180\mu\text{m}$, and (intensity) full-width-half-maximum (FWHM) pulse duration $\tau = 50$ fs. Each optical pulse in the longitudinal compression stage has an energy of 17.5 mJ, whereas each pulse in the transverse compression stage has an energy of about 26 mJ. Such specifications fall well within the realm of what is experimentally achievable today. The initial 30 keV electron pulse is a zero-emittance, uniformly-filled ellipsoid of diameter $28\mu\text{m}$ and length $14\mu\text{m}$, corresponding to a FWHM electron pulse duration of 100 fs. The particles are non-interacting and our simulation results are thus applicable to single-electron pulses. Although actual electron pulses have non-zero emittances that vary depending on factors like the type of emission mechanism used [6,43], we use electron pulses with zero initial emittance to perform numerical evaluations of our scheme that are independent of non-idealities in the initial electron pulse.

Figs. 3(b)-(d) depict the numerically-computed phase space distributions of electron pulses immediately after the longitudinal compression stage, for various optical incidence angles θ_1 . The longitudinal magnification M_l is defined as $M_l \equiv \sigma_z(t_f)/\sigma_z(0)$, where $\sigma_z = \sigma_z(t)$ is the standard deviation in z at time t . Here, $t = 0$ is defined as the instant captured in Fig. 3 (a)(ii) and $t = t_f$ the instant when the longitudinal focus is achieved (i.e. when M_l is minimized, captured in Fig. 3 (a)(iii)). The transverse magnification at the longitudinal focus is $M_{tl} \equiv \sigma_x(t_f)/\sigma_x(0)$, where $\sigma_x = \sigma_x(t)$ is the standard deviation in x at time t . In Fig. 3(b), we see two undesirable effects of normal optical incidence in the lab frame, both as analytically predicted in (14): the significant modulation in the transverse phase planes, and the substantial smear in the $\Delta\beta_z$ - Δz phase plane, resulting in a large longitudinal emittance and consequently a weak longitudinal compression factor $C_l \equiv M_l^{-1}$. The smeared particle distributions are largely due to walk-off between the center of the ponderomotive potential well and the center of the electron pulse, whereas the presence of transverse modulation is largely due to the oblique optical incidence angle in the rest frame of the electron pulse.

Note that the smearing and transverse modulation exist in spite of the fact that the optical pulse duration $\tau = 50$ fs is several tens of times smaller than w_0/v ($w_0(v\tau)^{-1} \approx 36 \gg 1$), and so nominally satisfies the thin lens approximation condition prescribed in [17] for normal incidence. This suggests that the thin lens approximation condition alone is not sufficient for effective longitudinal compression when the kinetic energy is on the order of 30 keV or greater.

As (14) predicts, injecting the optical pulse at an oblique angle according to (1) decouples the longitudinal modulation from the transverse modulation at the lowest

order and significantly improves the compression factor from the normal incidence case in Fig. 3(b). This is shown in Fig. 3(c), where we achieve a compression factor of $C_1 = 729$, taking the 100 fs electron pulse well into the attosecond regime. Further decreasing the incidence angle, as we do in Fig. 3(d), gives rise again to the substantial smearing of particle distributions in the $\Delta\beta_z$ - Δz phase plane, as well as modulations in the transverse phase planes. The sensitivity of the longitudinal compression to the optical incidence angle in the lab frame is further illustrated in Fig. 4(a).

Note that the area occupied in a 2-dimensional phase plane is not conserved in the interaction due to inter-dimensional coupling caused by a non-zero magnetic field. This does not violate Liouville's theorem, which states that the 6-dimensional phase space volume is conserved in a Hamiltonian system. Note also that the electron pulse is affected equally in the $\Delta\beta_x$ - Δx and $\Delta\beta_y$ - Δy phase planes due to our use of both Pulses I and II in Fig. 1(a), instead of attempting the longitudinal compression with only one of them.

Figs. 3(e)-(g) depict the numerically-computed phase space distributions of electron pulses immediately after the transverse compression stage, for various optical incidence angles θ_t . The transverse magnification is defined as $M_t \equiv \sigma_x(t_{ft})/\sigma_x(0)$, where t_{ft} is the time at which M_t is minimal. The longitudinal magnification at the transverse focus is $M_{lt} \equiv \sigma_z(t_{ft})/\sigma_z(0)$. Note that because the configuration in Fig. 1(a) subjects the electron pulse to similar treatments in x and y at the lowest order, σ_y behaves essentially in the same way as σ_x . The increase in $\Delta\beta_{x,y}$ (and subsequent decrease in t_{ft}) as θ_t decreases is as analytically predicted in (19). Although the transverse compression ratio is a relatively weak function of θ_t , we see in Fig. 4(b) that the choice of θ_t can significantly affect the longitudinal compression ratio in a three-dimensional compression scheme via higher-order terms of the transverse compression stage, with maximum longitudinal compression achieved when $\theta_t = 0^\circ$.

Figs. 4 (c) and (d) show the sensitivity of the compression to the displacement of the bunch centroid from the intensity minimum during the interaction. For the cases considered, one should aim to keep θ_1 within 0.1° of its optimal value, and the electron bunch centroid within $0.01w_0$ of the intensity minimum (values approximated by considering the half-width-half-maximum of the compression).

Using the simulation parameters of Fig. 3(c) in (15), we obtain $\Delta v_l \approx 3.925 \times 10^{-6}c$ at $\Delta z = -6.627 \mu\text{m}$ (actual value $\Delta\beta_z = 3.894 \times 10^{-6}$, relative error 0.80%). For the transverse compression cases, (19) yields $\Delta v_t \approx 3.671 \times 10^{-6}c$ at $\Delta x = -6.945 \mu\text{m}$ in Fig. 3(e) (actual value $\Delta\beta_x = 3.644 \times 10^{-6}$, relative error 0.74%); $\Delta v_t \approx 4.113 \times 10^{-6}c$ at $\Delta x = -6.944 \mu\text{m}$ in Fig. 3(f) (actual value $\Delta\beta_x = 4.081 \times 10^{-6}$, relative error 0.78 %); and $\Delta v_t \approx 5.010 \times 10^{-6}c$ at $\Delta x = -6.943 \mu\text{m}$ in Fig. 3(g) (actual value $\Delta\beta_x = 4.974 \times 10^{-6}$, relative error 0.72 %). These examples demonstrate the accuracy of (15) and (19) in estimating the velocity chirp induced by the interaction.

While the momentum modulations in these examples are small, they are still more than two orders of magnitude greater than the minimum momentum spread required by the Heisenberg uncertainty principle for the electron pulse dimensions considered

($\Delta x \Delta p_x \geq \hbar/2$ gives $\Delta \gamma \beta_x \geq 1.4 \times 10^{-8}$ for $\Delta x = 14 \mu\text{m}$). Nevertheless, actually producing an electron bunch with an emittance small enough for the bunch to be affected by such small modulations is currently very challenging (required emittance $\epsilon_x \sim \Delta x \Delta \gamma \beta_x < 0.1 \text{ nm}$). In actual implementations, larger momentum modulations – and hence more realistic emittance requirements – are readily achievable by, for instance, increasing the laser intensity (e.g., by tighter focusing) or introducing more stages in the cascade of Fig. 1(b). For single-electron sources in the tens-of-keV range, emittances as low as 3 nm have been demonstrated [43].

The negative velocity chirp in Fig. 3(c) causes the 30 keV electron pulse to compress longitudinally as it continues propagating after the interaction. Fig. 5(a) shows the evolution of the electron pulse's transverse and longitudinal standard deviations with time. Note that the transverse spread remains practically unchanged from its initial value, even as the electron pulse is compressed from a pulse duration of 100 fs to one of 137 as ($C_l = 729$). The electron pulse distribution at the longitudinal focus, marked by a vertical dotted line in Fig. 5(a), is shown in Figs. 5(b) and (c). The higher-order non-linear components of the induced velocity chirp prevents the ellipsoid from collapsing into a perfectly flat pancake.

Figs. 5(d), (e) and (f) depict the three-dimensional compression of a 30 keV electron pulse from a duration of 100 fs and a diameter of $28 \mu\text{m}$ to a duration of 137 as and a diameter of $0.153 \mu\text{m}$ ($C_l = 729$, $C_t = 183$). θ_l satisfies (1) and $\theta_t = 0^\circ$. Note that simultaneous transverse and longitudinal compression is achieved without affecting the longitudinal compression ratio of the purely-longitudinal-compression scheme in Fig. 5(a).

Fig. 6 depicts the transverse compression of a 30 keV, 1 fs electron pulse from a diameter of $28 \mu\text{m}$ to one of $0.156 \mu\text{m}$ ($C_t = 179$). $\theta_t = 0^\circ$ here. In Fig. 6(a), we see that the longitudinal spread remains practically unchanged from its initial value even as the electron pulse is focused transversely to a very small spot. This demonstrates the ability of the proposed scheme to focus ultrashort electron pulses without inducing temporal resolution-limiting distortions in them.

The $U w_0^{-4}$ dependence in (13) and (17) implies that significant energy savings are possible with tighter focusing. Decreasing the beam waist radius, however, enhances higher-order distortions that limit the maximum achievable compression. Fig. 7 illustrates the tradeoff between compression factor and pulse energy for the value of $U w_0^{-4}$ and the electron pulse used in Figs. 3 and 5. That the magnification scales as w_0^{-2} is consistent with the fact that the dominant higher-order distortions scale as $O(\epsilon_d^2)$ in (15) and (19). In Fig. 7, U refers to the total energy used in the longitudinal compression stage. Since $\theta_t = 0^\circ$, one may infer from (19) that the energy used for compression in each transverse dimension is typically smaller by a factor of about $(1 + \beta)$ so that the longitudinal and transverse foci coincide in the three-dimensional compression scheme. Fig. 7 shows that decent compression factors are already attainable with relatively low-energy optical pulses. In Fig. 7(a), for instance, a longitudinal compression factor of 20 is already achievable with optical pulses of waist radius $30 \mu\text{m}$ and total energy $27 \mu\text{J}$.

Although we have focused on single-electron pulses in this work, the proposed scheme can also be used for multi-electron pulse compression. This is especially (but not only) true when the electron pulse approximates a uniformly-filled ellipsoid or contains a linear velocity chirp. It should be noted, however, that typical multi-electron pulses have much larger diameters – which are on the order of a few hundreds of μm – than the electron pulses considered here, necessitating more energetic optical pulses to achieve the same compression qualities and focal times.

5. Conclusion

We have proposed an all-optical three-dimensional electron pulse compression scheme. The scheme comprises a succession of Hermite-Gaussian optical modes that effectively fashions a three-dimensional optical trap in the electron pulse's rest frame. Compression in each Cartesian dimension can be controlled without affecting electron pulse properties in orthogonal dimensions, at the lowest order. We showed mathematically that the right choice of optical incidence angle is necessary in longitudinal compression so that the induced velocity change is not a function of transverse coordinates and not accompanied by transverse phase plane modulations, at the lowest order. Although the transverse compression ratio is a relatively weak function of θ_t for 30 keV electrons, the choice of θ_t can significantly affect the longitudinal compression ratio in a three-dimensional compression scheme, with maximum longitudinal compression achieved when $\theta_t = 0^\circ$. We also derived analytical expressions approximating the net velocity change induced in a charged particle by a Hermite-Gaussian optical pulse of arbitrary order and incidence angle. These analytical expressions can be used to estimate the velocity chirp acquired by an electron pulse as a result of the laser-electron interaction.

Finally, using optical pulses that are realizable experimentally, we numerically demonstrated the longitudinal compression of a 30 keV electron pulse from 100 fs to 137 as (729 times compression), the three-dimensional compression of a 30 keV electron pulse from a duration of 100 fs and a diameter of $28\ \mu\text{m}$ to a duration of 137 as (729 times compression) and a diameter of $0.153\ \mu\text{m}$ (183 times compression), and the transverse compression of a 1 fs long, 30 keV electron pulse from a diameter of $28\ \mu\text{m}$ to one of $0.156\ \mu\text{m}$ (179 times compression). Even larger compression factors are potentially possible with larger beam waists, at the cost of focal time for a given optical pulse energy. Our energy scaling studies show that a compression factor of 20 is already achievable with a $27\ \mu\text{J}$ optical pulse of waist radius $30\ \mu\text{m}$. The required pulse energies may be lowered further still with the cascade scheme of Fig. 1(b).

The proposed scheme is useful in ultrafast electron imaging for both single- and multi-electron pulse compression, and as a means of focusing ultrashort electron pulses without inducing temporal resolution-limiting distortions in them. Broader applications of the mechanism studied here potentially include compressing or focusing accelerated protons [44] and neutral atoms [45], enhancing the quantum degeneracy of electron packets [46], creating flat electron beams [47], and creating ultrashort electron bunches

for coherent terahertz emission [48].

Acknowledgments

This work was partially supported by the U.S. Army Research Office Contract No. W911NF-13-D-0001, and the DARPA Young Faculty Award Grant No. D13AP00050. L.J.W. acknowledges support from the Agency for Science, Technology and Research, Singapore. T. R. acknowledges support from the Alexander von Humboldt Foundation, Germany.

References

- [1] P. Emma et al. First lasing and operation of an angstrom-wavelength free-electron laser. *Nat. Photon.*, 4:641–647, 2010.
- [2] A. P. Mancuso et al. Coherent imaging of biological samples with femtosecond pulses at the free-electron laser flash. *New J. Phys.*, 12:035003, 2010.
- [3] G. Sciaini and R. J. D. Miller. Femtosecond electron diffraction: heralding the era of atomically resolved dynamics. *Rep. Prog. Phys.*, 74:096101, 2011.
- [4] A. H. Zewail. 4d ultrafast electron diffraction, crystallography, and microscopy. *Annu. Rev. Phys. Chem.*, 57:65–103, 2006.
- [5] J. R. Dwyer, C. T. Hebeisen, R. Ernstorfer, M. Harb, V. B. Deyirmenjian, R. E. Jordan, and R. J. D. Miller. Femtosecond electron diffraction: making the molecular movie. *Phil. Trans. R. Soc. A*, 364:741–778, 2006.
- [6] F. Carbone, P. Musumeci, O. J. Luiten, and C. Hebert. A perspective on novel sources of ultrashort electron and x-ray pulses. *Chem. Phys.*, 392:1–9, 2012.
- [7] B. J. Siwick, J. R. Dwyer, R. E. Jordan, and R. J. D. Miller. Ultrafast electron optics: Propagation dynamics of femtosecond electron packets. *J. Appl. Phys.*, 92:1643–1648, 2002.
- [8] A. M. Michalik and J. E. Sipe. Analytic model of electron pulse propagation in ultrafast electron diffraction experiments. *J. Appl. Phys.*, 99:054908, 2006.
- [9] B. W. Reed. Femtosecond electron pulse propagation for ultrafast electron diffraction. *J. Appl. Phys.*, 100:034916, 2006.
- [10] Y. Wang and N. Gedik. Electron pulse compression with a practical reflectron design for ultrafast electron diffraction. *IEEE J. Sel. Top. Quant.*, 18:140–147, 2012.
- [11] M. Gao, H. Jean-Ruel, R. R. Cooney, J. Stampe, M. de Jong, M. Harb, G. Sciani, G. Moriena, and R. J. D. Miller. Full characterization of rf compressed femtosecond electron pulses using ponderomotive scattering. *Opt. Express*, 20:12048–12058, 2012.
- [12] T. van Oudheusden, P. L. E. M. Pasmans, S. B. van der Geer, M. J. de Loos, M. J. van der Wiel, and O. J. Luiten. Compression of subrelativistic space-charge-dominated electron bunches for single-shot femtosecond electron diffraction. *Phys. Rev. Lett.*, 105:264801, 2010.
- [13] G. H. Kassier, N. Erasmus, K. Haupt, I. Boshoff, R. Siegmund, S. M. M. Coelho, and H. Schwoerer. Photo-triggered pulsed cavity compressor for bright electron bunches in ultrafast electron diffraction. *Appl. Phys. B*, 109:249–257, 2012.
- [14] R. P. Chatelain, V. R. Morrison, C. Godbout, and B. J. Siwick. Ultrafast electron diffraction with radio-frequency compressed electron pulses. *Appl. Phys. Lett.*, 101:081901, 2012.
- [15] A. Gliserin, A. Apolonski, F. Krausz, and P. Baum. Compression of single-electron pulses with a microwave cavity. *New J. Phys.*, 14:073055, 2012.
- [16] P. Baum and A. H. Zewail. Attosecond electron pulses for 4d diffraction and microscopy. *P. Natl. Acad. Sci. USA.*, 104:18409–18414, 2007.

- [17] S. A. Hilbert, C. Uiterwaal, B. Barwick, H. Batelaan, and A. H. Zewail. Temporal lenses for attosecond and femtosecond electron pulses. *P. Natl. Acad. Sci. USA.*, 106:10558–10563, 2009.
- [18] M. Aidelsburger, F. O. Kirchner, F. Krausz, and P. Baum. Single-electron pulses for ultrafast diffraction. *P. Natl. Acad. Sci. USA.*, 107:19714–19719, 2010.
- [19] A. H. Zewail. Four-dimensional electron microscopy. *Science*, 328:187–193, 2010.
- [20] L. Veisz, G. Kurkin, K. Chernov, V. Tarnetsky, A. Apolonski, F. Krausz, and E. Fill. Hybrid dc–ac electron gun for fs-electron pulse generation. *New J. Phys.*, 9:56694, 2007.
- [21] C. Weninger and P. Baum. Temporal distortions in magnetic lenses. *Ultramicroscopy*, 113:145–151, 2012.
- [22] L. Novotny, E. J. Sánchez, and X. S. Xie. Near-field optical imaging using metal tips illuminated by higher-order hermite–gaussian beams. *Ultramicroscopy*, 71:21–29, 1998.
- [23] S.-C. Chu, Y.-T. Chen, K.-F. Tsai, and K. Otsuka. Generation of high-order hermite-gaussian modes in end-pumped solid-state lasers for square vortex array laser beam generation. *Opt. Express*, 20:7128–7141, 2012.
- [24] J. H. Eberly, J. Javanainen, and K. Rzażewsk. Above-threshold ionization. *Phys. Rep.*, 204:331–83, 1991.
- [25] H. A. H. Boot and R. B. R.-S. Harvie. Charged particles in a non-uniform radio-frequency field. *Nature*, 180:1187, 1957.
- [26] A. Ashkin. Optical trapping and manipulation of neutral particles using lasers. *P. Natl. Acad. Sci. USA*, 94:4853–4860, 1997.
- [27] I. Y. Dodin and N. J. Fisch. Particle manipulation with nonadiabatic ponderomotive forces. *Phys. Plasmas*, 14:055901, 2007.
- [28] G. V. Stupakov and M. S. Zolotarev. Ponderomotive laser acceleration and focusing in vacuum for generation of attosecond electron bunches. *Phys. Rev. Lett.*, 86:5274–5277, 2001.
- [29] B. J. Siwick, A. A. Green, C. T. Hebeisen, and R. J. D. Miller. Characterization of ultrashort electron pulses by electron-laser pulse cross correlation. *Opt. Lett.*, 30:1057–1059, 2005.
- [30] C. T. Hebeisen, R. Ernstorfer, M. Harb, T. Dartigalongue, R. E. Jordan, and R. J. D. Miller. Femtosecond electron pulse characterization using laser ponderomotive scattering. *Opt. Lett.*, 31:3517–3519, 2006.
- [31] V. Morrison, R. P. Chatelain, C. Godbout, and B. J. Siwick. Direct optical measurements of the evolving spatio-temporal charge density in ultrashort electron pulses. *Opt. Express*, 21:29–37, 2013.
- [32] M. Harb R. Ernstorfer T. Dartigalongue S. G. Kruglik C. T. Hebeisen, G. Sciaini and R. J. D. Miller. Grating enhanced ponderomotive scattering for visualization and full characterization of femtosecond electron pulses. *Opt. Express*, 16:3334–3341, 2008.
- [33] E. Esarey, P. Sprangle, M. Pilloff, and J. Krall. Theory and group velocity of ultrashort, tightly focused laser pulses. *J. Opt. Soc. Am. B*, 12:1695–1703, 1995.
- [34] Y. Harada and T. Asakura. Radiation forces on a dielectric sphere in the rayleigh scattering regime. *Opt. Communications*, 124:529–541, 1996.
- [35] L. Mandel and E. Wolf. *Optical Coherence and Quantum Optics*. Cambridge University Press, 1995.
- [36] J. D. Jackson. *Classical Electrodynamics*, 2nd ed. Wiley, New York, 1975.
- [37] O. Steuernagel. Optical lenses for atomic beams. *Phys. Rev. A*, 79:013421, 2009.
- [38] W. H. Press, S. A. Teukolsky, W. T. Vetterling, and B. P. Flannery. *Numerical Recipes in C*, 2nd ed. Cambridge University Press, 1992.
- [39] C. J. R. Sheppard. Polarization of almost-plane waves. *J. Opt. Soc. Am. A*, 17:335–341, 2000.
- [40] A. April. Ultrashort, strongly focused laser pulses in free space. In F. J. Duarte, editor, *Coherence and Ultrashort Pulse Laser Emission*, pages 355–382. InTech, 2010.
- [41] L. J. Wong, F. X. Kärtner, and S. G. Johnson. Improved beam waist formula for ultrashort, tightly focused linearly, radially, and azimuthally polarized laser pulses in free space. *Opt. Lett.*, 39:1258–1261, 2014.

- [42] A. April. Nonparaxial elegant laguerre-gaussian beams. *Opt. Lett.*, 33:1392–1394, 2008.
- [43] P. Baum. On the physics of ultrashort single-electron pulses for time-resolved microscopy and diffraction. *Chem. Phys.*, 423:55–61, 2013.
- [44] L. Robson, P. T. Simpson, R. J. Clarke, K. W. D. Ledingham, F. Lindau, O. Lundh, T. McCanny, P. Mora, D. Neely, C.-G. Wahlström, M. Zepf, and P. McKenna. Scaling of proton acceleration driven by petawatt-laser-plasma interactions. *Nat. Phys.*, 3:58–62, 2007.
- [45] U. Eichmann, T. Nubbemeyer, H. Rottke, and W. Sandner. Acceleration of neutral atoms in strong short-pulse laser fields. *Nature*, 461:1261–1264, 2009.
- [46] J. C. H. Spence, W. Qian, and M. P. Silverman. Electron source brightness and degeneracy from fresnel fringes in field emission point projection microscopy. *J. Vac. Sci. Technol. A*, 12:542–547, 1994.
- [47] J. Zhu, P. Piot, D. Mihalcea, and C. R. Prokop. Formation of compressed flat electron beams with high transverse-emittance ratios. *Phys. Rev. ST Accel. Beams*, 17:084401, 2014.
- [48] Y. Li and K.-J. Kim. Nonrelativistic electron bunch train for coherently enhanced terahertz radiation sources. *Appl. Phys. Lett.*, 92:014101, 2008.

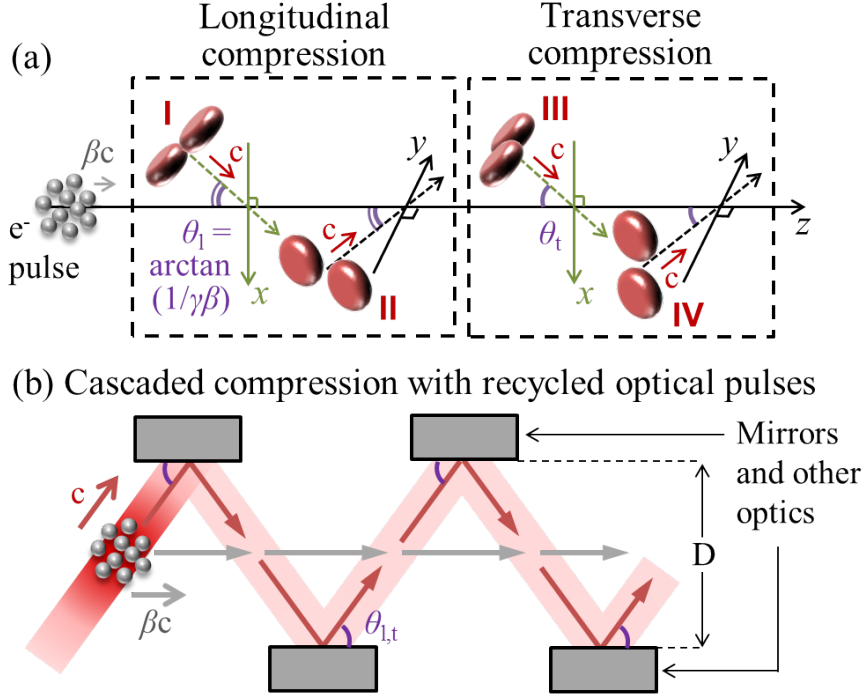


Figure 1. (a) Schematic diagram of three-dimensional electron pulse compression technique using pulsed first-order Hermite-Gaussian optical modes, which are portrayed as pairs of shiny red lozenges. Green lines lie in the x-z plane, black lines in the y-z plane. Dotted lines are the beam axes down which the optical pulses propagate. The electron pulse travels at speed $v \equiv \beta c$ in the +z-direction, c being the speed of light in vacuum. $\gamma \equiv (1 - \beta^2)^{-1/2}$ is the Lorentz factor. (b) Schematic diagram illustrating how a single optical pulse may be used to implement a succession of compression stages. Lines ending in filled arrowheads sketch the trajectories of optical (red) and electron (gray) pulses, with the arrowheads terminating at the interaction points.

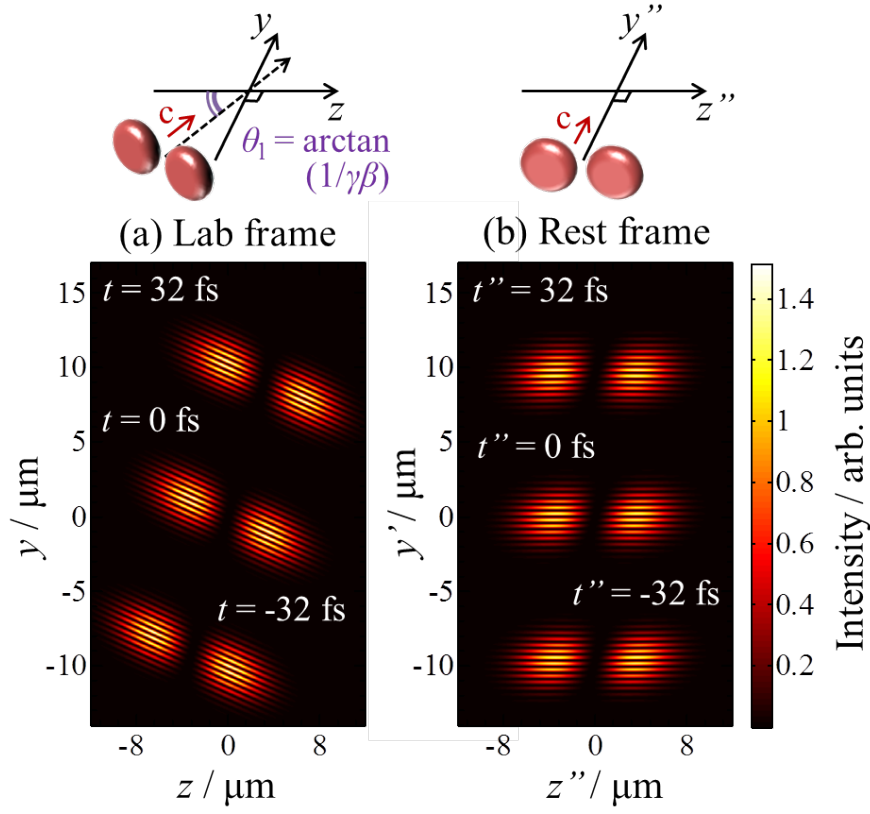


Figure 2. Intensity profile of Pulse II (c.f. Fig. 1(a)) at three instances in time in the (a) lab frame and (b) rest frame of a 30 keV electron pulse. In the lab frame, the temporal pulse and carrier wavefront are obliquely incident at $\theta_1 = 70.9^\circ$, in accordance with (1), giving rise to normal incidence in the rest frame. Double-primes denote rest frame variables.

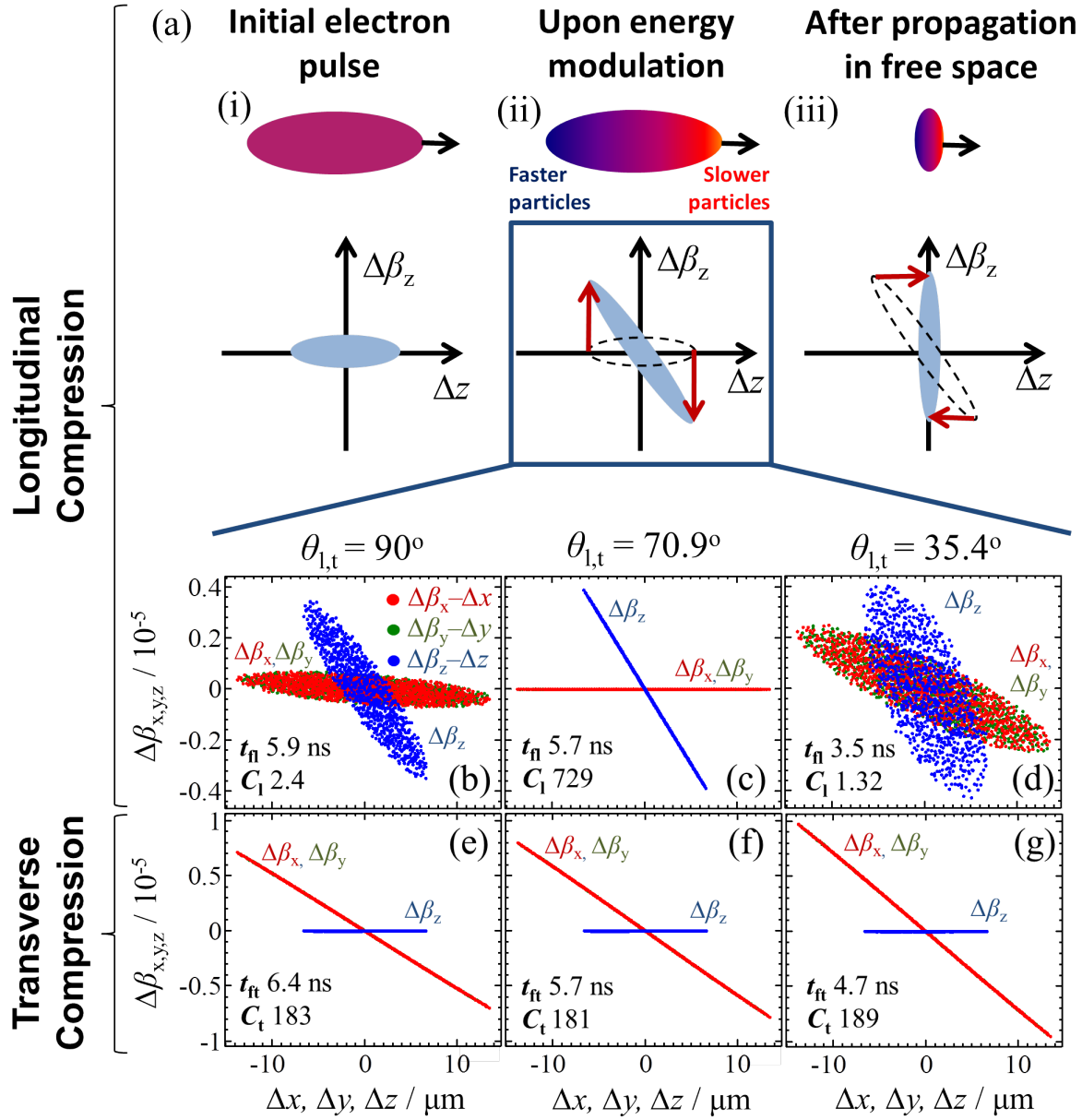


Figure 3. (a) Physical mechanism of the longitudinal compression scheme: (i) the initial electron pulse has a finite spread in momentum and position; (ii) the laser-electron interaction accelerates the back electrons and decelerates the front electrons; (iii) As the pulse propagates, the back electrons catch up with the front electrons, leading to electron pulse compression. $\Delta z \equiv z - \langle z \rangle$ denotes the particle's displacement from the bunch centroid along the z -dimension (and so on for the other variables). Phase plane distributions of the 30 keV electron pulse immediately after the longitudinal compression stage are shown for optical incidence angles (b) $\theta_l = 90^\circ$, (c) $\theta_l = \arctan(1/\gamma\beta) = 70.9^\circ$, and (d) $\theta_l = 35.4^\circ$. Phase plane distributions of the electron pulse immediately after the transverse compression stage are shown for optical incidence angles (e) $\theta_t = 90^\circ$, (f) $\theta_t = 70.9^\circ$ and (g) $\theta_t = 35.4^\circ$. Focal times $t_{fl,ft}$ and compression ratios $C_{l,t}$ are indicated for each case. 1000 particles were used in each simulation.

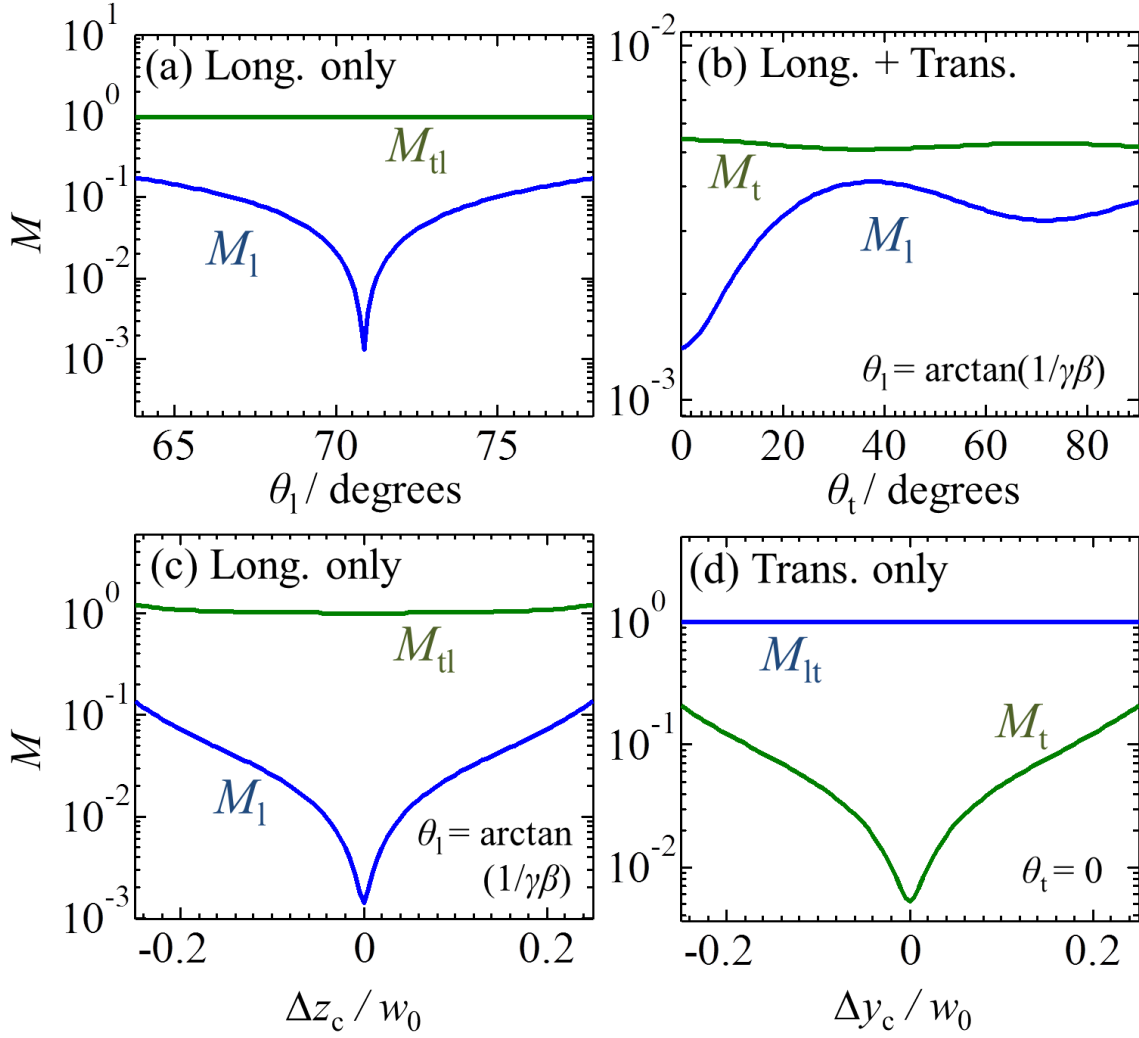


Figure 4. Sensitivity of compression ratios to (a) θ_l in a longitudinal compression scheme, (b) θ_t in a three-dimensional compression scheme, (c) longitudinal displacement Δz_c of the bunch centroid from the intensity minimum in a longitudinal compression scheme, and (d) transverse displacement Δy_c of the bunch centroid from the intensity minimum in a transverse compression scheme (along y).

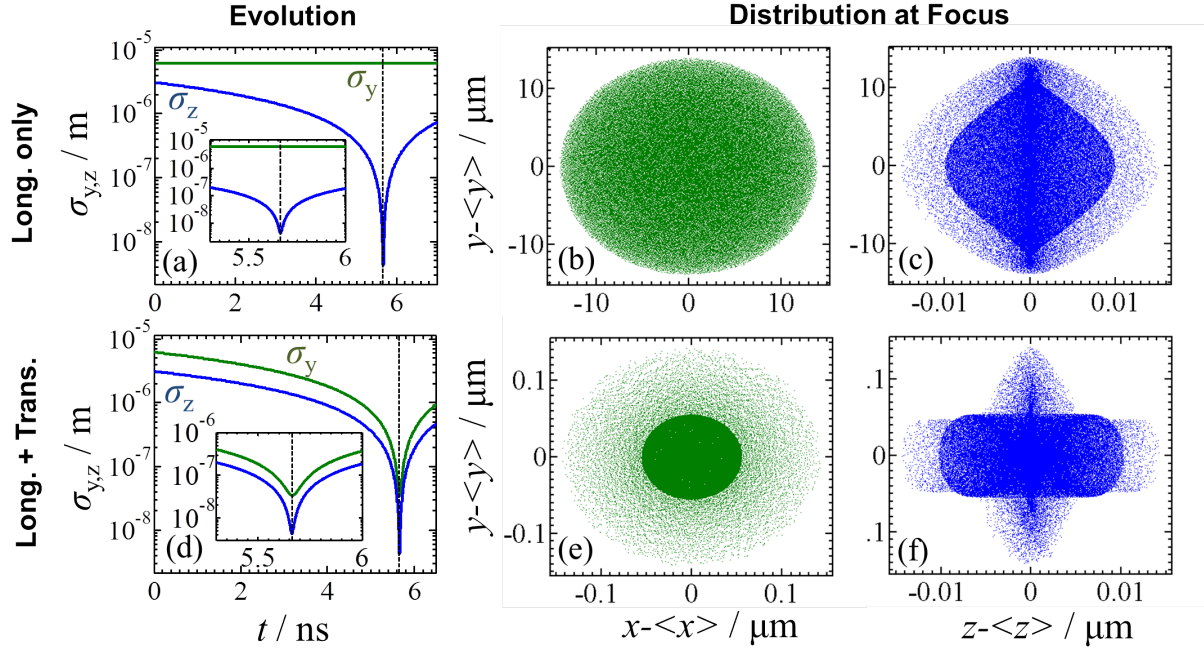


Figure 5. Longitudinal compression of a 30 keV electron pulse from 100 fs to 137 as (longitudinal compression factor $C_1 = 729$): (a) Evolution of standard deviations in y and z, and corresponding spatial distributions at the longitudinal focus (vertical dotted line in (a)) in the (b) y-x and (c) y-z planes. Three-dimensional compression of a 30 keV electron pulse from a duration of 100 fs and a diameter of $28 \mu\text{m}$ to a duration of 137 as and an effective diameter of $0.153 \mu\text{m}$ ($C_1 = 729$, $C_t = 183$): (d) Evolution of standard deviations in y and z, and corresponding spatial distributions at the focus (vertical dotted line in (d)) in the (e) y-x and (f) y-z planes. 10^5 particles were used in each simulation. In (a) and (d), the standard deviation in x was omitted as it practically lies over that in y.

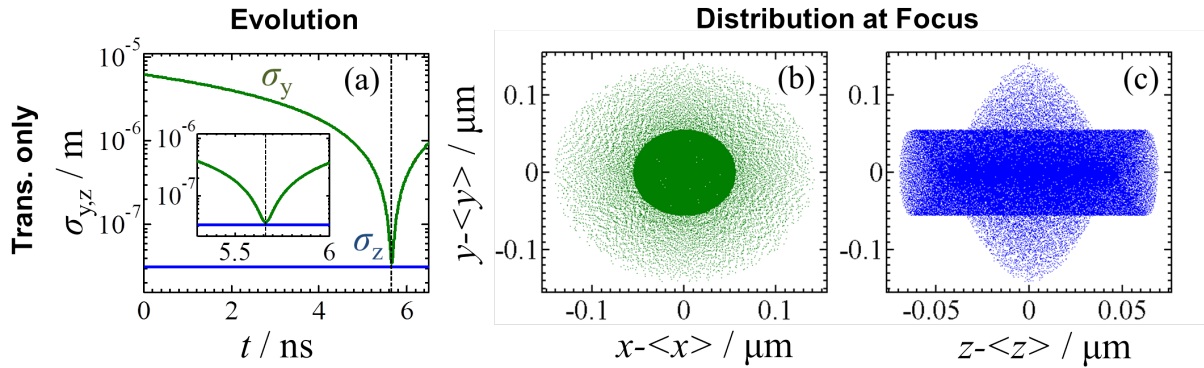


Figure 6. Transverse compression of a 30 keV, 1 fs-long electron pulse from a diameter of $28 \mu\text{m}$ to an effective diameter of $0.156 \mu\text{m}$ (transverse compression factor $C_t = 179$): (a) Evolution of standard deviations in y and z, and corresponding spatial distributions at the transverse focus (vertical dotted line in (a)) in the (b) y-x and (c) y-z planes.

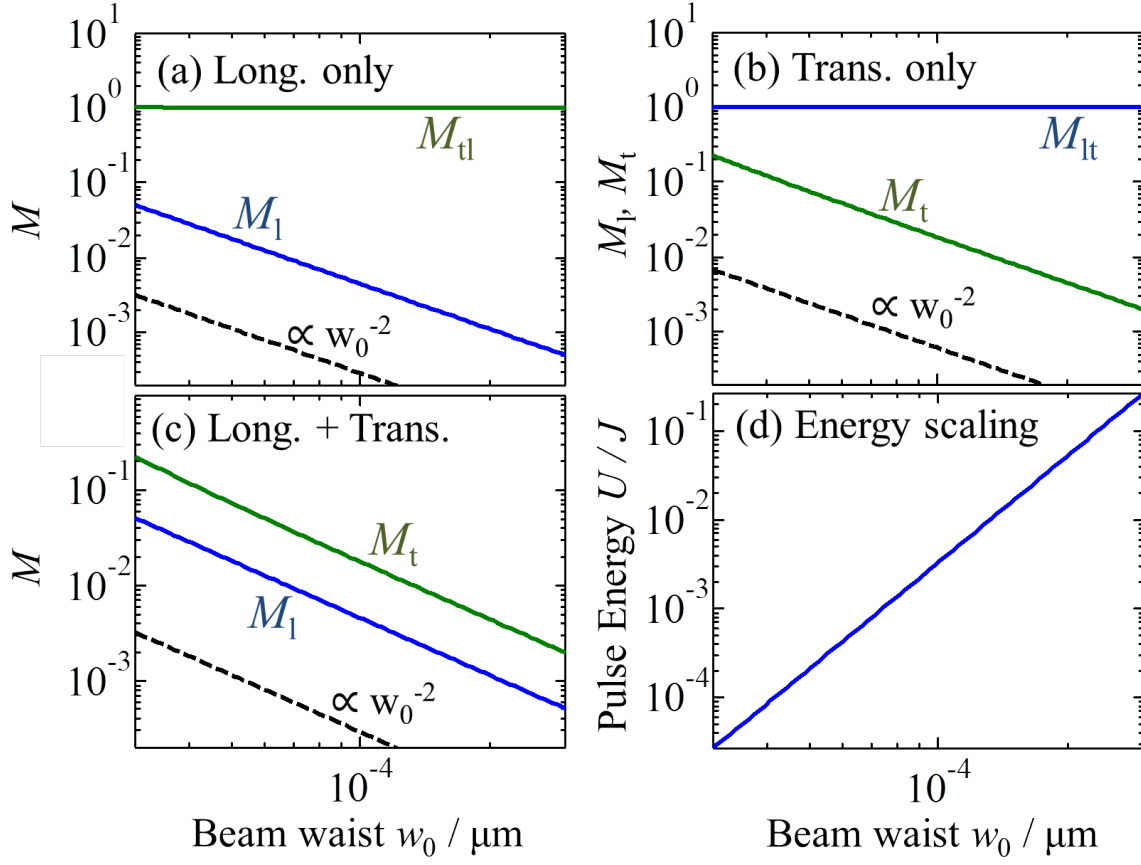


Figure 7. Scaling of magnification with optical beam waist for the optical and electron pulses of Figs. 3 and 5: (a) Longitudinal compression only (b) Transverse compression only and (c) Three-dimensional compression. (d) plots the scaling of energy U with beam waist w_0 when Uw_0^{-4} is kept constant, from $U = 27 \mu\text{J}$ at $w_0 = 30 \mu\text{m}$ to $U = 270 \text{ mJ}$ at $w_0 = 300 \mu\text{m}$. θ_l satisfies (1) and $\theta_t = 0^\circ$.